Available online at www.sciencedirect.com
SCIENCE DIRECT®
Journal of Sound and Vibration 284 (2005) 733–755
JOURNAL OF SOUND AND VIBRATION
www.elsevier.com/locate/jsvi

Electromechanical interaction in rotordynamics of cage induction motors

Timo P. Holopainen[a,*], Asmo Tenhunen[b], Antero Arkkio[b]

[a] *VTT Technical Research Centre of Finland, VTT Industrial Systems, P.O. Box 13022, FIN-02044 VTT, Finland*
[b] *Helsinki University of Technology, Laboratory of Electromechanics, P.O. Box 3000, FIN-02015 HUT, Finland*

Received 11 November 2003; received in revised form 5 May 2004; accepted 8 July 2004
Available online 18 November 2004

Abstract

Eccentric rotor motion induces an unbalanced magnetic pull between the rotor and stator of cage induction motors. Recently, a linear parametric model of this eccentricity force due to the arbitrary rotor motion was presented. The purpose of this study is to combine this electromagnetic force model with a simple mechanical rotor model, and further, to demonstrate the rotordynamic response induced by this electromechanical interaction. An electromechanical rotor model is derived on the basis of the Jeffcott rotor with two additional variables for the harmonic currents of the rotor cage. Applying this model, the rotordynamic effects of electromechanical interaction were studied. Three induction motors were used in the numerical examples. The electromechanical parameters of these motors were estimated from the numerical simulations carried out separately. The results obtained show that the electromechanical interaction may decrease the natural frequencies of the rotor, induce additional damping or cause rotordynamic instability. These interaction effects are most significant in motors operating at or near the first bending critical speed. Excluding the potential rotordynamic instability, the numerical results indicate that the electromechanical interaction reduces effectively the unbalance response close to the first bending critical speed.

*Corresponding author. ABB Oy, Electrical Machines, P.O. Box 186, FIN-00381 Helsinki, Finland. Tel.: +358 50 33 22488, fax: +358 10 22 22141.
E-mail address: timo.holopainen@fi.abb.com (T.P. Holopainen).

0022-460X/$ - see front matter © 2004 Elsevier Ltd. All rights reserved.
doi:10.1016/j.jsv.2004.07.007

Nomenclature

$\mathbf{A}$	system matrix
$\underline{a}$	unbalance vector
a_{p-1}, a_{p+1}	force model parameters
$\hat{B}_p$	amplitude for the fundamental component of the magnetic flux density
$\hat{B}_h$	effective amplitude for the high-order components of the magnetic flux density
c_{p-1}, c_{p+1}	force model parameters
d	external viscous damping coefficient
d_r	outer diameter of the rotor
$e_{p\pm1}^{\mathrm{rms}}$, e_F^{rms}	error measures for cage-current components and electromagnetic force
$\underline{F}$	excitation force
$\underline{F}_e$	electromagnetic force
$\underline{G}_F$, $\underline{G}_{p\pm1}$	frequency response functions
$\hat{\underline{i}}_{p-1}$, $\hat{\underline{i}}_{p+1}$	space-vector variables for cage-current components
k	shaft stiffness coefficient
k_e	electromagnetic force parameter
k_{p-1}, k_{p+1}	coupling factors due to the leakage flux and saturation
L	self-inductance of one rotor-cage mesh
L_{p-1}, L_{p+1}	rotor-cage inductances for cage-current components
l_e	equivalent core length
m	mass of rotor core
N_p	number of points
N_s	number of samples
P	output power
p	number of pole-pairs of the motor
$\underline{p}_c$	centre-point position of the rotor
$\underline{q}_{p-1}$, $\underline{q}_{p+1}$	transformed variables related to the cage-current components
$\mathbf{q}$	state vector
R_{p-1}, R_{p+1}	rotor-cage resistances for cage-current components
R_ω	speed ratio
s	slip of the rotor with respect to the fundamental component of the stator field
T_e	electromagnetic torque
T_s	length of sample
T_{sim}	length of simulation period
t	time
U	supply voltage
$\mathbf{u}_i$	eigenvector i
α	ratio between the apparent electromagnetic stiffness and the shaft stiffness
β	direction of the pulse at its starting instant
γ	parameter associated with the slip and number of pole-pairs
δ_e	equivalent air-gap length including slotting
δ_i	decay constant of eigenvalue i
Δ	length of the pulse
ε	relative amplitude of the pulse
ζ	factor for external viscous damping
ϑ_{b0}	phase angle for the space vector of the magnetic flux density
$\underline{\lambda}_i$	eigenvalue i
μ_0	permeability of free space
τ_{p-1}, τ_{p+1}	time constants for cage-current components
ω	angular frequency
ω_n	natural bending frequency of the rotor
ω_s	supply frequency
ω_p	angular velocity of the pulse
Ω_m	rotational speed of rotor
$\underline{x}$	complex number
$\underline{x}^*$	complex conjugate of $\underline{x}$
$\hat{\underline{x}}$	space vector
$\tilde{x}$	dimensionless equivalent to x
$\lvert\underline{x}\rvert$	magnitude of complex number $\underline{x}$
$\check{\underline{x}}$	discrete Fourier transform of time sequence of $\underline{x}$
$\underline{x}^r$, $\underline{x}^s$	complex number in rotor or stator reference frame
$x_{,t}$	differentiation of x with respect to time
x_{rat}	value of x in rated operation conditions

1. Introduction

Electromagnetic fields in the air gap of an electric machine produce electromagnetic forces between the rotor and stator. The total force exerted on the rotor due to the eccentric rotor position is called the unbalanced magnetic pull. This eccentricity force is directed roughly over the shortest air gap. At low frequencies, the vibration amplitudes of flexural modes may be large enough to couple the electromagnetic system with the mechanical one. This electromechanical interaction changes the vibration characteristics of the motor; for example, it may decrease the critical speeds of the machine, induce additional damping or cause rotordynamic instability. Thus, to control the vibrations and rotordynamic behaviour of electric machines, it is important to predict the effects of electromechanical interaction between the rotor and stator.

The electromagnetic field in the air gap encircling the rotor can be divided into the spatial harmonic components. The main and strongest component is the fundamental component, which is required for torque generation. The order of this component is the same as the number of pole-pairs of the machine, p. An eccentric rotor position together with the fundamental field component produces two additional field components in particular. The order of these components, $p \pm 1$, differs with one from the order of the fundamental component. The main part of the eccentricity force is produced by these additional field components together with the fundamental field. This description is complicated to some extent due to the equalising currents of the rotor cage. While these harmonic currents are induced by the eccentric rotor position together with the fundamental field, they themselves can induce the same field components and decrease the total eccentricity force exerted on the rotor.

Freise and Jordan [1] derived the analytical equations for the unbalanced magnetic pull in static and dynamic eccentricity. Further, they introduced the coefficients for the force reduction induced by the equalising currents of the rotor cage. Finally, they presented a simple formula to determine the first critical speed starting from the negative spring coefficient induced by the electromagnetic field. Früchtenicht et al. [2] derived an analytic model for the unbalanced magnetic pull when the rotor is in a circular whirling motion with an arbitrary whirling frequency. They applied the assumption that the currents and fluxes vary sinusoidally in time. Using this model they determined the additional stiffness and damping coefficients induced by the electromagnetic fields, and developed an electromechanical model to study the effects on the rotordynamic stability. Belmans et al. [3] investigated analytically and experimentally the flexible shaft induction motors. Their calculation model resembled that of Früchtenicht et al. [2], but they focused on two-pole machines. They concluded that a potential reason for the rotordynamic instability results from the electromagnetic damping coefficient which may be negative. The approach of Skubov and Shumakovich [4] enabled an arbitrary motion of the rotor. They applied the averaging method together with the Lagrange formulation for the analytical derivation of the equations. They discovered that the tangential component of the electromagnetic total force might be the reason for the instability. The references given above, as well as most of the former studies, apply analytical approaches to investigate the electromechanical interaction. However, the saturation of magnetic materials, and stator and rotor slottings, may be difficult to model by analytical means.

Arkkio et al. [5] studied the electromagnetic force exerted on the rotor of a cage induction motor. They determined numerically the unbalanced magnetic pull in circular whirling motion as a function of whirling frequency. They validated the numerical results with the experimental

measurements using a rigid rotor and two magnetic bearings to generate the controlled whirling motion. Starting from the frequency response function, Arkkio et al. [5] identified a parametric model for the total electromagnetic force. However, the parameters of this model are not clearly related to the analytical equations derived previously or to the machine characteristics. To meet this need, Holopainen et al. [6] derived the required analytical equations for the unbalanced magnetic pull due to the arbitrary rotor motion in transient operation. In this connection, they introduced separate variables for the essential harmonics of the rotor cage currents, which enabled the assumption of arbitrary rotor motion.

Previous research on this issue has not been conclusive, in part because it has generally been based on the stiffness and damping coefficients induced by the electromagnetic fields, when an adequate force model requires independent variables for the harmonic cage currents. The main purpose of the present investigation was to derive an electromechanical rotor model for cage induction motors with physical parameters, which can be estimated from numerical simulation results. In addition, the second aim was to present the main rotordynamic consequences induced by the electromechanical interaction.

The approach of this study is purely theoretical. Numerical simulation models are applied to estimate the electromagnetic parameters of the example motors. Otherwise, only the analytical derivations and simple mathematical models are used to reveal the essential behaviour of the electromechanical interaction. Further, the aim is to find the general form of the equations. Thus, the mechanical model was kept very simple and the mechanical damping was assumed to be viscous in character. Moreover, the rotor and stator axes were assumed to remain parallel during the rotor motions, which simplified the analyses.

The present study was limited to cage induction motors without parallel paths in the stator windings. These parallel paths are assumed to induce additional electromagnetic forces by enabling circulatory currents in the stator winding resembling the effects of rotor cage currents. Further, the homopolar flux, which may be associated with the eccentricity, and may have a central effect on the rotordynamics of two-pole motors [3], was neglected. Moreover, the parametric force model applied in this study included only two low-order components of the electromagnetic fields in the air gap. There are reasons to remember that there are high-order components contributing to the total force. An example of the simulation results revealing the effect of high-order components on the unbalanced magnetic pull is shown in Ref. [5].

2. Methods

2.1. Mechanical rotor model

The mechanical behaviour of the system was modelled by the most simple rotor model consisting of two degrees-of-freedom describing the deflection of the shaft. This model is commonly called a Laval shaft or Jeffcott rotor. The rotor core was modelled as a rigid cylinder located at the middle of a uniform, massless, flexible shaft. The shaft was simply supported at its ends by the rigid frictionless bearings. The gravitational force exerted on the rotor was neglected. The mechanical damping was assumed external and viscous in character. In most cases, this mechanical damping was neglected to emphasise the effects of electromagnetic forces. The

cylindrical rotor was assumed to move only in the transversal plane or, more precisely, in the xy -plane in the stator reference frame. The origin of this frame was located in the centre of the stator bore and it was assumed to coincide with the rotational axis of the bearings. The position of the rotor-core centre was defined by a complex variable $\underline{p}_c^s$, where the bar under the symbol denotes the complex quantity and the superscript s refers to the stator reference frame. The equations of motion of this simple rotor can be written using the complex formulation [7]

$$m\underline{p}_{c,tt}^s + d\underline{p}_{c,t}^s + k\underline{p}_c^s = \underline{F}^s(t), \tag{1}$$

where m is the mass of the rotor core, d the external viscous damping, k the shaft stiffness, $\underline{F}^s$ the excitation force; the time derivative is denoted by subscript t after a comma.

The equations were mainly derived in the rotor reference frame. This frame is rotating with the same angular velocity as the rotor. The origin of this rotor reference frame is fixed to the origin of the stator reference frame, although the centre point of the rotor may travel along an eccentric path. The Jeffcott rotor equation with unbalance force excitation can be written in the rotor reference frame with a constant rotational speed [7]

$$m\underline{p}_{c,tt}^r + (d + \mathrm{j}2m\Omega_m)\underline{p}_{c,t}^r + \left(k + \mathrm{j}d\Omega_m - m\Omega_m^2\right)\underline{p}_c^r = \Omega_m^2 m\,\underline{a}, \tag{2}$$

where Ω_m is the rotational speed of the rotor and $\underline{a}$ the unbalance vector; superscript r refers to the rotor reference frame.

2.2. Simulation of electromagnetic system

The simulation of the electromagnetic system was based on the time-stepping, finite-element analysis. The details of the method are presented by Arkkio [8]. The rotor and stator axes were assumed perpendicular to the xy-plane, and the magnetic field in the core region of the motor was assumed two-dimensional, parallel to the xy-plane. End winding impedances were used in circuit equations of the windings to model approximately the end effects. The laminated iron core was treated mostly as a non-conducting, magnetically non-linear medium, and the non-linearity was modelled by a single-valued magnetisation curve. The motion of the rotor was obtained by moving the centre point of the rigid rotor and changing the finite-element mesh in the air gap. In addition, the rotor was rotated at the mechanical angular velocity.

The field and circuit equations were discretized and solved together. First- or second-order, isoparametric, triangular elements were used for the electromagnetic fields. The initial state for the simulation was determined employing the time-harmonic analysis. The time-dependence of the variables was modelled by the Crank–Nicholson method. The magnetic field and the cage currents were obtained directly in the solution of equations. The method presented by Coulomb [9] was used for computing the electromagnetic force.

2.3. Electromagnetic force model

Our starting point was the parametric force model presented in detail by Holopainen et al. [6]. Here, only the main equations and parameters are introduced. The space vector formulation [10] was applied to present the distributed variables as the harmonic cage-current components and the

voltages of the stator windings. The parametric force model, including two differential equations for the cage-current harmonics, and one equation for the total electromagnetic force, can be written in the rotor reference frame [6]

$$\begin{aligned}
&\hat{\underline{i}}^r_{p-1,t} + \tau^{-1}_{p-1}\hat{\underline{i}}^r_{p-1} + a_{p-1}\left((\underline{p}^r_{c,t})^* + \mathrm{j}s\omega_s(\underline{p}^r_c)^*\right)\mathrm{e}^{\mathrm{j}(s\omega_s t+\vartheta_{b0})} = 0,\\
&\hat{\underline{i}}^r_{p+1,t} + \tau^{-1}_{p+1}\hat{\underline{i}}^r_{p+1} + a_{p+1}\left(\underline{p}^r_{c,t} + \mathrm{j}s\omega_s\underline{p}^r_c\right)\mathrm{e}^{\mathrm{j}(s\omega_s t+\vartheta_{b0})} = 0,\\
&\underline{F}^r_e(t) = k_e\underline{p}^r_c + c_{p-1}(\hat{\underline{i}}^r_{p-1})^*\mathrm{e}^{\mathrm{j}(s\omega_s t+\vartheta_{b0})} + c_{p+1}\hat{\underline{i}}^r_{p+1}\mathrm{e}^{-\mathrm{j}(s\omega_s t+\vartheta_{b0})},
\end{aligned} \tag{3}$$

where $\hat{\underline{i}}^r_{p-1}$ and $\hat{\underline{i}}^r_{p+1}$ are the space vectors of the harmonic components $p \pm 1$ of the cage currents, the circumflex above a symbol refers to the space-vector character, p is the number of pole pairs, the asterix $(*)$ denotes the complex conjugate, ω_s is the electrical supply frequency, s is the slip of the rotor with respect to the fundamental component of the stator field, ϑ_{b0} is the phase angle of the magnetic-flux-density space-vector at $t = 0$, $\underline{F}^r_e$ is the total electromagnetic force exerted on the rotor, and finally $a_{p\pm1}$, $\tau_{p\pm1}$, $c_{p\pm1}$ and k_e are the system parameters. In this paper, these parameters are estimated from the simulation results. To reveal the relation of these parameters to the machine and operation characteristics, the analytical formulas can be written using several simplifying assumptions [6]

$$\begin{aligned}
a_{p\pm1} &= \frac{Lk_{p\pm1}}{2\mu_0 L_{p\pm1}}\,\hat{B}_p, \qquad & c_{p\pm1} &= \frac{\pi d_r l_e k_{p\pm1}}{4\delta_e}\,\hat{B}_p,\\
k_e &= \frac{\pi d_r l_e}{4\mu_0\delta_e}\left(\hat{B}^2_p + \hat{B}^2_h\right), & \tau_{p\pm1} &= \frac{L_{p\pm1}}{R_{p\pm1}},
\end{aligned} \tag{4}$$

where μ_0 is the permeability of air, d_r the outer diameter of the rotor core, l_e the equivalent core length, δ_e the equivalent air-gap length including slotting, L the self-inductance of one mesh of the rotor cage, $k_{p\pm1}$ the coupling factors due to the leakage flux and saturation, $\tau_{p\pm1}$, $R_{p\pm1}$, and $L_{p\pm1}$ the time constants, the resistances, and the total inductances of the rotor cage determined separately for the harmonic components $p \pm 1$, respectively, $\hat{B}_p$ the amplitude of the fundamental component of the magnetic flux density in the air gap, and $\hat{B}_h$ the effective amplitude of all the high-order harmonics [6]. In steady-state operation $\hat{B}_p$ and $\hat{B}_h$ and, thus, the analytical parameters of Eq. (4) are constant.

2.4. Parameter estimation of electromagnetic force model

The parameters of the electromagnetic force model, $a_{p\pm1}$, $\tau_{p\pm1}$, $c_{p\pm1}$ and k_e, were estimated from the frequency response function (FRF). The system was excited with a short impulse and the response was simulated numerically. The applied method is closely related to the experimental methods used to identify the vibration characteristics of a system [11]. The approach used in this study is presented in detail by Holopainen et al. [12]. The excitation is produced by moving the rotor from its concentric position for a short period of time. The induced cage-current harmonics and the electromagnetic total force are calculated in the time domain. Using spectral analysis techniques, the FRF between these responses and excitation are determined. The discrete FRF between the electromagnetic force and rotor motion is obtained

from the formula

$$\underline{G}_F(\mathrm{j}\omega_i) = \frac{\underline{\check{F}}_e^r(\mathrm{j}\omega_i)}{\underline{\check{p}}_c^r(\mathrm{j}\omega_i)}, \quad \omega_i = 2\pi i/T_s, \quad i = 0, \pm 1, \pm 2, \ldots, \tag{5}$$

where $\underline{\check{F}}_e$ and $\underline{\check{p}}_c$ are the discrete Fourier transforms of the electromagnetic force and rotor displacement signals, respectively. The length of the sample T_s and the total number of the data points determine the frequency resolution. The parameters of the electromagnetic force model were estimated in two phases from the simulated FRFs using a curve-fitting procedure, which was based on the least-squares fit and on the iterative search of the denominator terms [12].

The covered frequency range depends on the length and type of the excitation pulse [11]. In previous studies [12–14], the rotor was moved in the radial direction in the stator reference frame. In this study, we applied a rotating excitation pulse in order to control better the excitation frequency range, and thus, excite more effectively the required system modes. The type of the pulse was

$$\underline{p}_c^s(t) = \begin{cases} \dfrac{\varepsilon\delta_e}{2}\left(1 - \cos\dfrac{2\pi(t-t_1)}{\Delta}\right)\mathrm{e}^{\mathrm{j}\{\omega_p(t-t_1)+\beta\}}, & t_1 < t < t_1 + \Delta, \\ 0, & \text{otherwise}, \end{cases} \tag{6}$$

where ε is the relative pulse amplitude, t_1 the starting time of the pulse, Δ the length of the pulse, ω_p the angular velocity of the pulse, and β the direction of the pulse at its starting instant.

The two-pole induction motors, differing from the motors with more poles, may have in a whirling motion a strong unsynchronous force component. For example, the static eccentricity of the rotor induces this force component at twice the supply frequency in the stator reference frame. The origin of this force component is the magnetic field components induced by the stator slotting together with the eccentricity field components $p \pm 1$. This additional force component makes the parameter estimation more difficult, because the system parameters are time-dependent. An attractive remedy for this is the averaging method [11]. In this method, a set of FRFs obtained by different test parameters is averaged. In the two-pole machines, the spatial wavelength of the disturbing field producing the unsynchronous force component is 2π. Thus, in this study, a set of samples (= time-histories) was generated using the evenly distributed starting direction of the pulse. All the other test parameters were kept equal. The formula for the pulse direction in the sample i was

$$\beta_i = \frac{1}{2}\frac{2\pi}{p}\frac{i-1}{N_s}, \quad i = 1, 2, \ldots, N_s, \tag{7}$$

where N_s is the total number of samples.

2.5. Electromechanical rotor model

The differential equations of Eq. (3) include the time-dependent multiplier $\mathrm{e}^{\mathrm{j}s\omega_s t}$. To get rid of this multiplier, each of the space-vector variables is transformed using the formulas

$$\begin{aligned} \underline{q}_{p-1}^r &= (\hat{\underline{i}}_{p-1}^r)^* \mathrm{e}^{\mathrm{j}(s\omega_s t + \vartheta_{b0})}, \\ \underline{q}_{p+1}^r &= \hat{\underline{i}}_{p+1}^r \mathrm{e}^{-\mathrm{j}(s\omega_s t + \vartheta_{b0})}. \end{aligned} \tag{8}$$

These new variables are related to the respective harmonic components of cage currents, but they are not space-vectors. Substituting these new variables into Eq. (3) yields a set of equations without explicit time-dependency

$$\begin{aligned}
&\underline{q}^r_{p-1,t} + \left(\tau^{-1}_{p-1} - \mathrm{j}s\omega_s\right)\underline{q}^r_{p-1} + a_{p-1}\left(\underline{p}^r_{c,t} - \mathrm{j}s\omega_s\underline{p}^r_c\right) = 0,\\
&\underline{q}^r_{p+1,t} + \left(\tau^{-1}_{p+1} + \mathrm{j}s\omega_s\right)\underline{q}^r_{p+1} + a_{p+1}\left(\underline{p}^r_{c,t} + \mathrm{j}s\omega_s\underline{p}^r_c\right) = 0,\\
&\underline{F}^r_e(t) = k_e\underline{p}^r_c + c_{p-1}\underline{q}^r_{p-1} + c_{p+1}\underline{q}^r_{p+1}.
\end{aligned} \tag{9}$$

The electromechanical rotor equations are obtained by combining the mechanical equations of motion (2) with the electromagnetic force model of Eq. (9)

$$\begin{aligned}
&m\underline{p}^r_{c,tt} + (d + \mathrm{j}2m\Omega_m)\underline{p}^r_{c,t} + \left(k - k_e + \mathrm{j}d\Omega_m - m\Omega^2_m\right)\underline{p}^r_c - c_{p-1}\underline{q}^r_{p-1} - c_{p+1}\underline{q}^r_{p+1} = \Omega^2_m m\,\underline{a},\\
&\underline{q}^r_{p-1,t} + \left(\tau^{-1}_{p-1} - \mathrm{j}s\omega_s\right)\underline{q}^r_{p-1} + a_{p-1}\left(\underline{p}^r_{c,t} - \mathrm{j}s\omega_s\underline{p}^r_c\right) = 0,\\
&\underline{q}^r_{p+1,t} + \left(\tau^{-1}_{p+1} + \mathrm{j}s\omega_s\right)\underline{q}^r_{p+1} + a_{p+1}\left(\underline{p}^r_{c,t} + \mathrm{j}s\omega_s\underline{p}^r_c\right) = 0.
\end{aligned} \tag{10}$$

2.6. Non-dimensional rotor model

To minimize the number of parameters and emphasise the essential behaviour of the system, the electromechanical rotor model of (10) was transformed into a non-dimensional form using the dimensionless variables and time

$$\tilde{\underline{p}}^r_c = \frac{\underline{p}^r_c}{\delta_e}, \quad \tilde{\underline{q}}^r_{p\pm1} = \frac{c_{p\pm1}}{k\delta_e}\,\underline{q}^r_{p\pm1}, \quad \tilde{t} = \omega_n t, \tag{11}$$

where the tilde above a symbol refers to a dimensionless quantity, and $\omega_n = \sqrt{k/m}$ is the natural bending frequency of the rotor. Substituting the new variables into Eq. (10) yields

$$\begin{aligned}
&\tilde{\underline{p}}^r_{c,\tilde{t}\tilde{t}} + 2(\zeta + \mathrm{j}R_\omega)\tilde{\underline{p}}^r_{c,\tilde{t}} + \left(1 - \alpha + \mathrm{j}2\zeta R_\omega - R^2_\omega\right)\tilde{\underline{p}}^r_c - \tilde{\underline{q}}^r_{p-1} - \tilde{\underline{q}}^r_{p+1} = R^2_\omega\tilde{\underline{a}},\\
&\tilde{\underline{q}}^r_{p-1,\tilde{t}} + \left(\tilde{\tau}^{-1}_{p-1} - \mathrm{j}\gamma R_\omega\right)\tilde{\underline{q}}^r_{p-1} + \alpha\tilde{c}_{p-1}\left(\tilde{\underline{p}}^r_{c,\tilde{t}} - \mathrm{j}\gamma R_\omega\tilde{\underline{p}}^r_c\right) = 0,\\
&\tilde{\underline{q}}^r_{p+1,\tilde{t}} + \left(\tilde{\tau}^{-1}_{p+1} + \mathrm{j}\gamma R_\omega\right)\tilde{\underline{q}}^r_{p+1} + \alpha\tilde{c}_{p+1}\left(\tilde{\underline{p}}^r_{c,\tilde{t}} + \mathrm{j}\gamma R_\omega\tilde{\underline{p}}^r_c\right) = 0,
\end{aligned} \tag{12}$$

where the new dimensionless parameters are

$$\begin{aligned}
&R_\omega = \frac{\Omega_m}{\omega_n}, \quad \alpha = \frac{k_e}{k}, \quad \tilde{c}_{p\pm1} = \frac{a_{p\pm1}c_{p\pm1}}{k_e}, \quad \tilde{\tau}_{p\pm1} = \omega_n\tau_{p\pm1},\\
&\zeta = \frac{d}{2m\omega_n}, \quad \tilde{\underline{a}} = \frac{\underline{a}}{\delta_e}, \quad \gamma = \frac{s\omega_s}{\Omega_m} = \frac{ps}{1-s},
\end{aligned} \tag{13}$$

where R_ω is the speed ratio, α the ratio between the apparent electromagnetic stiffness and the shaft stiffness, ζ the factor for external viscous damping, and γ a shorthand notation associated with the slip and the number of pole-pairs. Eq. (12) is suitable for motors with two or more

pole-pairs ($p \geqslant 2$). When the number of pole-pairs is one, and the homopolar flux is neglected, the differential equations are reduced into the form

$$\begin{aligned} \underline{\tilde{p}}^r_{c,\tilde{t}\tilde{t}} + 2(\zeta + \mathrm{j}R_\omega)\underline{\tilde{p}}^r_{c,\tilde{t}} + \left(1 - \alpha + \mathrm{j}2\zeta R_\omega - R_\omega^2\right)\underline{\tilde{p}}^r_c - \underline{\tilde{q}}^r_{p+1} &= R_\omega^2 \underline{\tilde{a}}, \\ \underline{\tilde{q}}^r_{p+1,\tilde{t}} + \left(\tilde{\tau}^{-1}_{p+1} + \mathrm{j}\gamma R_\omega\right)\underline{\tilde{q}}^r_{p+1} + \alpha c_{p+1}\left(\underline{\tilde{p}}^r_{c,\tilde{t}} + \mathrm{j}\gamma R_\omega \underline{\tilde{p}}^r_c\right) &= 0. \end{aligned} \tag{14}$$

Eq. (14) is clearly a simplification of the actual electromechanical behaviour of two-pole motors, because the homopolar flux, corresponding to the $p-1$ term, may affect the rotordynamics and stability of the system significantly [3].

2.7. Rotordynamic stability

The stability of a linear system is determined by the eigenvalues of this system. Briefly, the system is stable, if the real parts of all the eigenvalues are positive [15]. To determine the eigenvalues, the system equations, i.e. the homogeneous part of Eq. (12), were first transformed into the form of state equations [15]

$$\tilde{\mathbf{q}}^r_{,\tilde{t}} = \tilde{\mathbf{A}}^r \tilde{\mathbf{q}}^r \tag{15}$$

with the dimensionless state vector

$$\tilde{\mathbf{q}}^r = \left\{ \underline{\tilde{p}}^r_c \quad \underline{\tilde{p}}^r_{c,\tilde{t}} \quad \underline{\tilde{q}}^r_{p-1} \quad \underline{\tilde{q}}^r_{p+1} \right\}^{\mathrm{T}} \tag{16}$$

and the system coefficient matrix

$$\tilde{\mathbf{A}}^r = \begin{bmatrix} 0 & 1 & 0 & 0 \\ -\left(1 - \alpha + \mathrm{j}2\zeta R_\omega - R_\omega^2\right) & -2(\zeta + \mathrm{j}R_\omega) & 1 & 1 \\ \mathrm{j}\alpha\tilde{c}_{p-1}\gamma R_\omega & -\alpha\tilde{c}_{p-1} & -\tilde{\tau}^{-1}_{p-1} + \mathrm{j}\gamma R_\omega & 0 \\ -\mathrm{j}\alpha\tilde{c}_{p+1}\gamma R_\omega & -\alpha\tilde{c}_{p+1} & 0 & -\tilde{\tau}^{-1}_{p+1} - \mathrm{j}\gamma R_\omega \end{bmatrix}. \tag{17}$$

The eigenvalue problem is

$$\left[\tilde{\mathbf{A}}^r - \underline{\tilde{\lambda}}^r \mathbf{I}\right]\tilde{\mathbf{u}}^r = \mathbf{0}, \tag{18}$$

where $\mathbf{I}$ is the identity matrix. The solution consists of four eigenvalues $\underline{\tilde{\lambda}}^r_i$ and associated eigenvectors $\tilde{\mathbf{u}}^r_i$ ($i = 1, 2, 3, 4$). These eigenvalues can be expressed in the general form

$$\underline{\tilde{\lambda}}^r_i = -\tilde{\delta}_i + \mathrm{j}\tilde{\omega}^r_i, \tag{19}$$

where $\tilde{\delta}_i$ is the dimensionless decay constant and $\tilde{\omega}^r_i$ is the non-dimensional frequency of the eigenvalue number i in the rotor reference frame. The dimensional eigenvalues are obtained from

the formula

$$\underline{\lambda}_i^r = \omega_n \tilde{\lambda}_i^r = -\tilde{\delta}_i \omega_n + \mathrm{j}\tilde{\omega}_i^r \omega_n = -\delta_i + \mathrm{j}\omega_i^r. \tag{20}$$

The eigenvalues of Eqs. (19) and (20) are given in the rotor reference frame. In the stator reference frame, the frequencies are

$$\tilde{\omega}_i^s = \tilde{\omega}_i^r + R_\omega, \quad \omega_i^s = \omega_i^r + \Omega_m. \tag{21}$$

Irrespective of the reference frame, the linear system is asymptotically stable, if all the eigenvalues have positive decay constant. Similar stability considerations can be carried out for the two-pole motors starting from Eq. (14).

2.8. Unbalance response

Usually, the most important excitation force of the system is the mass unbalance. When the rotor is rotating at constant angular velocity and the stability conditions are fulfilled, the unbalance excites a synchronous whirl of the rotor. This means that the unbalance and response vectors are rotating with the same angular velocity as the rotor.

Substituting this steady-state assumption in the rotor reference frame, i.e., $\underline{\tilde{p}}_{c,\tilde{i}}^r \equiv \underline{\tilde{q}}_{p\pm1,\tilde{i}}^r \equiv 0$, into Eq. (12) yields

$$\begin{aligned}
&\left(1 - \alpha + \mathrm{j}2\zeta R_\omega - R_\omega^2\right)\underline{\tilde{p}}_c^r - \underline{\tilde{q}}_{p-1}^r - \underline{\tilde{q}}_{p+1}^r = R_\omega^2 \underline{\tilde{a}},\\
&\left(\tilde{\tau}_{p-1}^{-1} - \mathrm{j}\gamma R_\omega\right)\underline{\tilde{q}}_{p-1}^r - \mathrm{j}\alpha\tilde{c}_{p-1}\gamma R_\omega \underline{\tilde{p}}_c^r = 0,\\
&\left(\tilde{\tau}_{p+1}^{-1} + \mathrm{j}\gamma R_\omega\right)\underline{\tilde{q}}_{p+1}^r + \mathrm{j}\alpha\tilde{c}_{p+1}\gamma R_\omega \underline{\tilde{p}}_c^r = 0.
\end{aligned} \tag{22}$$

The steady-state response of the cage-current harmonics, i.e. $\underline{\tilde{q}}_{p-1}^r$ and $\underline{\tilde{q}}_{p+1}^r$, can be solved from the two last equations. Substituting these into the first equation of Eq. (22) gives the amplification factor due to the unbalance

$$\frac{\underline{\tilde{p}}_c^r}{\underline{\tilde{a}}} = \frac{R_\omega^2}{1 - \alpha + \mathrm{j}2\zeta R_\omega - R_\omega^2 - \dfrac{\mathrm{j}\alpha\tilde{c}_{p-1}\gamma R_\omega \tilde{\tau}_{p-1}}{1 - \mathrm{j}\gamma R_\omega \tilde{\tau}_{p-1}} + \dfrac{\mathrm{j}\alpha\tilde{c}_{p+1}\gamma R_\omega \tilde{\tau}_{p+1}}{1 + \mathrm{j}\gamma R_\omega \tilde{\tau}_{p+1}}}. \tag{23}$$

3. Results

3.1. Example motors

The developed electromechanical rotor model was applied for three induction motors. The smallest one was a 15 kW four-pole motor investigated previously with numerical and experimental methods [5,12–14]. The second one was a large 2.6 MW two-pole motor with rated operation above its first bending critical speed. The third one was a large 4.25 MW four-pole motor with subcritical rated operation. The main parameters of these motors are given in Table 1. The effective mass and stiffness of the rotors were approximated starting from the design data of the first natural bending frequency together with the total mass of the rotor and the structural

arrangements. Fig. 1 shows, as an example, the cross-section of the 2.6 MW motor and a typical magnetic flux distribution during the operation.

3.2. Force model parameters

The numerical model of the 15 kW motor was generated using the second-order triangular elements, and a typical finite-element mesh contained about 8700 nodes. The larger motors were generated with first-order elements, while a typical element mesh of the 2.6 MW motor contained about 3500 nodes, and a mesh of the 4.2 MW motor about 4700 nodes. The parameters of the electromagnetic force model were estimated from the calculated impulse response data. The length of the simulation samples was systematically $T_{\text{sim}} = 2.0$ s. The number of time steps per one period of supply voltage was chosen to be 400. This yielded the time step length of 0.05 ms for the 15 kW motor at rated operation, and about 0.042 ms for the large machines.

The relative amplitude of the pulse was systematically $\varepsilon = 0.2$, and the length $\Delta = 0.04$ s. The starting time of the pulse was $t_1 = 0.067$ s for the large machines, and $t_1 = 0.08$ s for the 15 kW motor, in order to attenuate all initial transients of the system. For the 15 kW and 4.2 MW motors, the pulse was rotated with the angular velocity of the rotor, i.e., $\omega_p = \Omega_m$, and, for the 2.6 MW motor, with the angular velocity of the stator field, $\omega_p = \omega_s$. In the averaging, the number of samples for the 2.6 MW motor was chosen to be four, $N_s = 4$, and, for the other machines, $N_s = 1$. With these pulse parameters, the theoretical continuous excitation range was about $-50\text{ Hz} < f_{\text{exc}} < 50\text{ Hz}$ in the rotor reference frame.

The time domain data describing the excitation and response were transformed into the frequency domain. To obtain a reasonable calculation time, the number of points in the discrete Fourier transform was chosen to be systematically $n = 2^{14}$. To obtain a reasonable spectral resolution without extending the simulation time excessively, the sample size was lengthened by padding zeros at the end of the simulated data [11]. In addition, the initial phase before the pulse was systematically cut away before the transformation. To eliminate potential interpolation error, the sample time for the discrete Fourier transform was chosen to be a multiple of the simulation time-step length. For the 15 kW motor, it was 0.65 ms, and for the other motors, it was about 0.67 ms. This led to the total length of the sample $T_s \approx 11$ s, and to the spectral resolution about 0.1 Hz. The frequency response functions were generated without any additional numerical filtering.

The force model parameters were estimated from the frequency response functions using the curve-fitting procedure. All the data points with the absolute value of whirling frequency below $|f_w| < 25$ Hz in the rotor reference frame were used for the curve fitting. The error measure for the parametric curves was the root mean square compared to the original FRF of each case. The applied formulas for the relative error for harmonic currents and total force were

$$e_{p\pm1}^{\text{rms}} = \frac{1}{a_{p\pm1}} \sqrt{\frac{1}{N_p} \sum_{i=1}^{N_p} \left| \underline{G}_{p\pm1}^{\text{fit}}(\mathrm{j}\omega_i) - \underline{G}_{p\pm1}^{\text{frf}}(\mathrm{j}\omega_i) \right|^2},$$

$$e_F^{\text{rms}} = \frac{1}{k_0} \sqrt{\frac{1}{N_p} \sum_{i=1}^{N_p} \left| \underline{G}_F^{\text{fit}}(\mathrm{j}\omega_i) - \underline{G}_F^{\text{frf}}(\mathrm{j}\omega_i) \right|^2}, \tag{24}$$

where $|\omega_i| \leqslant 2\pi\ 25$ Hz.

Table 1
Main parameters of the example motors

Parameter	Motor		
	15 kW	2.6 MW	4.2 MW
Number of poles	4	2	4
Number of phases	3	3	3
Number of parallel paths	1	1	1
Outer diameter of stator core	235	860	1100 mm
Inner diameter of stator core	145	480	710 mm
Radial air-gap length	0.45	6.0	4.5 mm
Number of stator slots	36	48	48
Number of rotor slots	34	40	58
Skew of rotor slots	0	0	0
Connection	Delta	Star	Star
Rated voltage	380	4000	13200 V
Rated frequency	50	60	60 Hz
Rated current	28	417	217 A
Rated power	15	2600	4250 kW
Rotor effective mass	30	1100	2500 kg
Rotor effective stiffness	150	48	150 MN/m
Natural bending frequency	356	33.3	39.0 Hz
Rated slip	0.032	0.0038	0.0042

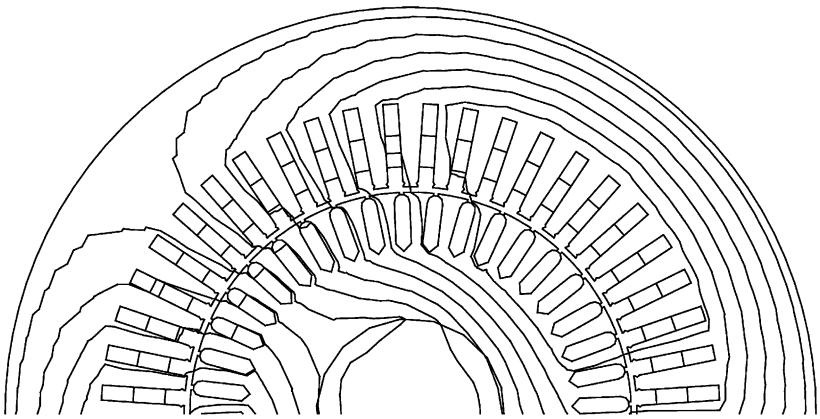

Fig. 1. Half of the cross-sectional geometry of the 2.6 MW motor and a typical flux distribution during operation.

Fig. 2 shows the calculated FRF between the force and whirling motion for the 15 kW motor. To illustrate the complex FRF, it is divided into the real-valued radial and tangential components. In addition, Fig. 2 shows the parametric FRF obtained by the curve-fitting procedure. The estimated parameter values for each motor are given in Table 2. The parameters, estimated in this

study for the 15 kW motor with a rotating excitation, are almost equivalent to the parameters estimated with a non-rotating excitation [12].

3.3. Rated operation

The dimensionless parameters of the corresponding electromechanical rotor models were determined using the data of Tables 1 and 2 together with Eq. (13). Table 3 shows the parameters of the example motors in the rated operation. The system equations were generated using these parameters and neglecting the external viscous damping. The eigenproblem of each motor was solved leading to three or four eigenvalues and associated eigenvectors. The imaginary part of an eigenvalue gives the dimensionless eigenfrequency, and the real part the opposite number of the dimensionless decay constant. Table 4 shows the eigenvalues in the stator reference frame. Two of the modes are associated with the eccentricity harmonics of the rotor cage currents, and two with the forward and backward whirling modes. However, all the modes have electromagnetic and mechanical contributions. As can be seen in Table 4, the electromechanical interaction decreases the eigenfrequencies of the whirling modes about 2.0%. The dimensionless decay constant of each of the modes and motors is small, varying between –0.03% and 0.64%. All the eigenvalues decay except the forward whirling mode of the 2.6 MW motor.

3.4. Effect of rotational speed

The parameters of the electromagnetic force model are dependent mainly on the rotational speed, supply voltage and loading torque. Further, the electromagnetic system is non-linear with respect to these operation parameters. Thus, to avoid excessive calculation, an upper limit curve was defined for the main operation parameters (Fig. 3). Below the rated operation point, this curve is a consequence of the saturation, which limits the amplitude of the magnetic flux density. Above the rated operation point, the available supply voltage is the limiting factor. A similar curve represents a typical control strategy when a frequency converter is used to control the operation parameters of an induction motor. Tables 5 and 6 show the dimensionless force parameters for the 2.6 and 4.2 MW motors, respectively, in several operation points on the upper limit curve. According to Tables 5 and 6, the parameters are relatively constant, when the rotational speed is lower than the rated speed. This follows from the fact that the constant torque operation corresponds to the constant flux operation [6]. When the rotational speed is higher than the rated speed, the change in the parameter values is more evident. These changes mean that the electromagnetic force induced by the eccentric motion is, in that case, lower.

The parameter values of the rated operation point were chosen to represent the typical parameters at variable operation speeds. Fig. 4 shows the dimensionless eigenvalues and decay constants of the 2.6 MW motor. Fig. 5 shows the corresponding curves for the 4.2 MW motor. Here, it can be mentioned that this four-pole motor is designed for the subcritical operation range. Figs. 4 and 5 show that two of the modes, the forward whirling mode and the electromagnetic mode $p+1$, couple strongly together close to the critical speed. The same figures show that the backward whirling mode does not couple with the electromagnetic modes. Actually, the rotation direction of the backward whirling mode is the reverse of the direction of the other modes. Further, Figs. 4 and 5 show that one of the coupled modes is unstable when the rotation speed is

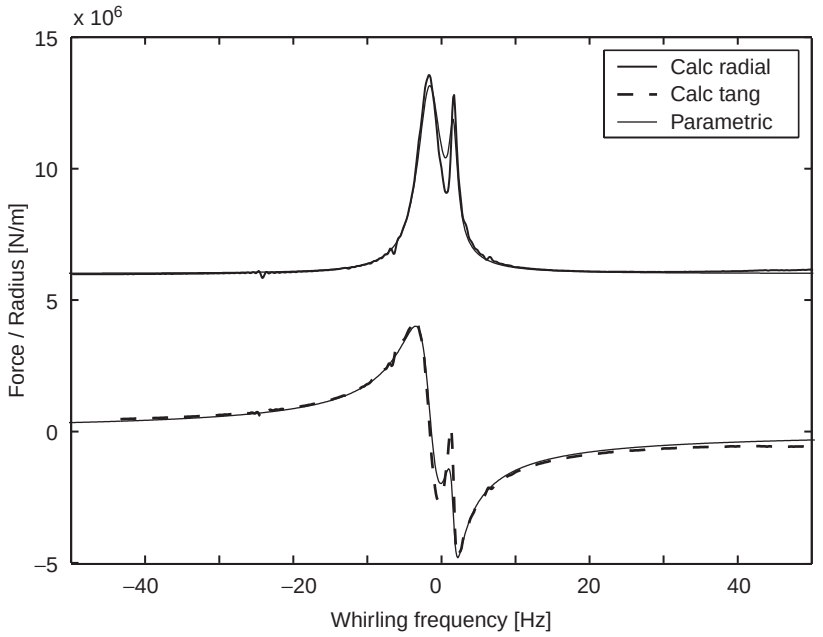

Fig. 2. FRF of the 15 kW motor in the rated operation as a function of whirling frequency in the rotor reference frame. The radial direction is defined in the direction of the shortest air gap and the tangential component perpendicular to the radial one.

Table 2
Estimated force parameters of the example motors in the rated operation conditions

Motor	Parameter							Relative error		
	a_{p-1} (kA/m)	a_{p+1} (kA/m)	τ_{p-1} (s)	τ_{p+1} (s)	k_0 (MN/m)	c_{p-1} (N/A)	c_{p+1} (N/A)	e_{p-1}^{rms} (%)	e_{p+1}^{rms} (%)	e_F^{rms} (%)
15 kW	367	353	0.229	0.079	16.8	10.7	19.5	12.3	4.7	2.4
2.6 MW	—	223	—	0.774	5.34	—	14.8	—	1.5	1.0
4.2 MW	302	274	1.151	0.807	20.1	8.40	45.1	6.4	1.8	1.4

Table 3
Dimensionless parameters of the electromechanical rotor model for the example motors

Motor	Parameter						
	R_ω	α	$\tilde{c}_{p-1}$	$\tilde{c}_{p+1}$	$\tilde{\tau}_{p-1}$	$\tilde{\tau}_{p+1}$	γ
15 kW	0.070	0.112	0.234	0.409	511	176	0.06610
2.6 MW	1.800	0.111	—	0.623	—	162	0.00379
4.2 MW	0.766	0.134	0.126	0.616	240	169	0.00844

Table 4
Dimensionless eigenvalues of the example motors at rated operation speed in the stator reference frame

Motor	Eigenvalue			
	bw	fw	$p-1$	$p+1$
15 kW	$-0.15\times10^{-3}-\mathrm{j}0.980$	$-0.17\times10^{-3}+\mathrm{j}0.980$	$-1.90\times10^{-3}+\mathrm{j}0.075$	$-5.41\times10^{-3}+\mathrm{j}0.065$
2.6 MW	$-0.08\times10^{-3}-\mathrm{j}0.979$	$+0.27\times10^{-3}+\mathrm{j}0.979$	—	$-6.36\times10^{-3}+\mathrm{j}1.793$
4.2 MW	$-0.16\times10^{-3}-\mathrm{j}0.983$	$-1.13\times\cdot10^{-3}+\mathrm{j}0.983$	$-3.97\times10^{-3}+\mathrm{j}0.772$	$-4.66\times10^{-3}+\mathrm{j}0.760$

The corresponding eigenmodes are the backward whirling (bw), the forward whirling (fw), and the cage-current harmonics- $p\pm1$.

higher than a certain limit close to the critical speed. This unstable mode is a combination of the forward whirling and the $p+1$ mode.

3.5. Electromechanical instability

As can be seen in Figs. 4 and 5 , the electromechanical interaction may destabilise one of the modes, and thus, the whole rotordynamic system. The stability is achieved by including the non-rotating damping into the model. The minimum damping value to eliminate the destabilising force on the entire speed range is $\zeta=0.018$ for the 2.6 MW motor, and $\zeta=0.022$ for the 4.2 MW motor. To reveal the effect of different parameters on the stability, it is possible to plot so-called stability charts. Fig. 6 shows, as an example, a stability chart based on the parameters of the 2.6 MW motor.

3.6. Response to unbalance

Fig. 7 shows an example of the amplification factor due to the mass unbalance. The parameters of the system correspond to those of the 2.6 MW motor. The maximum response occurs at speed ratio $R_\omega=0.955$. This speed, which might be called the critical speed, is 4.5% lower than the natural bending frequency of the rotor without electromechanical interaction. Further, as can be seen in Fig. 4a , the unbalance excitation at this speed ratio does not coincide with any of the dimensionless eigenfrequencies. Actually, the synchronous excitation frequency is between the eigenfrequencies of the forward whirling and $p+1$ modes. This means that the unbalance response is a combination of these two modes. In addition, according to Fig. 7, the electromechanical interaction reduces effectively the unbalance response close to the critical speed.

3.7. Meaning of main model parameters

The most important parameter affecting the eigenfrequencies of the system is α, the ratio between the electromagnetic stiffness coefficient and the mechanical stiffness. Fig. 8 shows the eigenfrequencies of the forward whirling mode and the mode $p+1$ with the three different values of α. The reference point for the other parameters is the rated operation point of the 2.6 MW

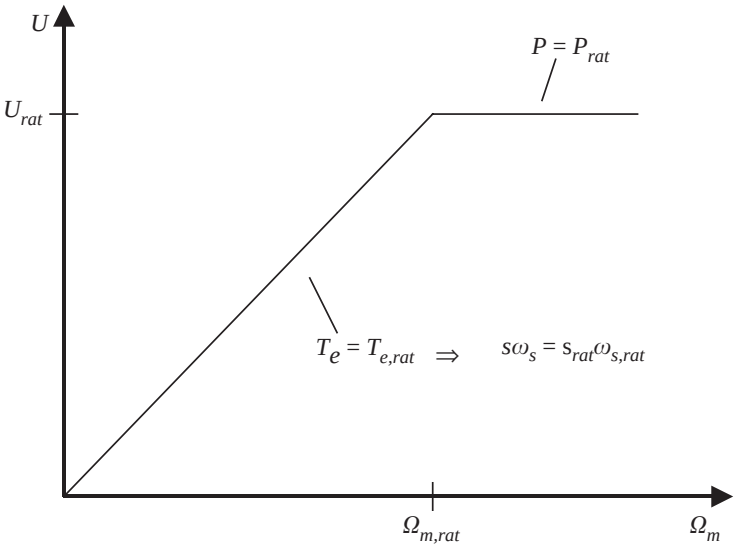

Fig. 3. The upper limit curve of main operation parameters as a function of rotational speed. The supply voltage is denoted by U, the output power by P , the electromagnetic torque by T_e, and the parameter values at the rated operation by subscript rat.

Table 5
Estimated force parameters for the 2.6 MW motor

Operation conditions				Parameter		
$\omega_s/\omega_{s,\mathrm{rat}}$	U/U_{rat}	R_ω	s	α	$\tilde{c}_{p+1}$	$\tilde{\tau}_{p+1}$
0.25	0.25	0.44	0.01520	0.1099	0.629	168.1
0.50	0.50	0.90	0.00760	0.1114	0.621	163.0
0.75	0.75	1.35	0.00507	0.1112	0.620	162.3
1.00	1.00	1.80	0.00380	0.1107	0.623	161.7
1.25	1.00	2.25	0.00400	0.0922	0.603	204.6

The presented points are on the upper limit curve of the operation parameters.

machine. The effect of α on the eigenfrequency of the backward whirling mode is similar to the forward whirling mode without coupling to the electromagnetic modes. This effect can be seen in Figs. 4 and 5 . The electromagnetic part of α, i.e., k_e, determines the electromagnetic force divided by the rotor eccentricity without the force reduction effect of the rotor-cage currents. Eq. (4) shows that the value of k_e is determined mainly by the flux density amplitude, the surface area of the rotor core, and the air-gap length.

Table 6
Estimated force parameters for the 4.2 MW motor

Operation conditions				Parameter				
$\omega_s/\omega_{s,\mathrm{rat}}$	U/U_{rat}	R_ω	s	α	$\tilde{c}_{p-1}$	$\tilde{c}_{p+1}$	$\tilde{\tau}_{p-1}$	$\tilde{\tau}_{p+1}$
0.25	0.25	0.189	0.01687	0.136	0.141	0.609	266	176
0.50	0.50	0.382	0.00840	0.135	0.131	0.613	249	171
0.75	0.75	0.574	0.00560	0.134	0.127	0.614	243	169
1.00	1.00	0.766	0.00420	0.134	0.126	0.616	240	169
1.25	1.00	0.958	0.00430	0.133	(0.241)	0.520	(460)	237
1.50	1.00	1.149	0.00450	0.097	(0.214)	0.474	(460)	247

The presented points are on the upper limit curve of the operation parameters. The values in parentheses are uncertain because the simple parametric force model cannot describe the simulated response of cage-current component $p-1$. However, the parameters together describe well the total electromagnetic force.

The coefficients $\tilde{c}_{p-1}$ and $\tilde{c}_{p+1}$ describe the coupling efficiency between the fundamental field and cage-current harmonics. Using physical reasoning, it is possible to conclude that $\tilde{c}_{p\pm1} \geqslant 0$ and $\tilde{c}_{p-1} + \tilde{c}_{p+1} < 1$. In our test examples, the sum of these parameters varied between 0.62 and 0.74 in the rated operation conditions (Table 3). The sum of these parameters determines the reduction of the electromagnetic force far off from the resonance frequencies roughly following the formula $\underline{F}_{e,0} = k_e(1 - \tilde{c}_{p-1} - \tilde{c}_{p+1})$. This can be seen comparing the curves in Fig. 2 and the parameters of Table 2.

The most important parameters affecting to the damping of the modes are the time constants $\tilde{\tau}_{p\pm1}$. The physical background of these parameters lay in the resistances and inductances of the corresponding harmonic components of the cage currents (see Eqs. (4) and (13)). Fig. 9 shows the decay constants of the forward whirling and $p+1$ modes with three different values for $\tilde{\tau}_{p+1}$. The reference point for the other parameters is the rated operation point of the 2.6 MW machine. It can be emphasised that the modes in Fig. 9 are coupled, and that the forward whirling and $p+1$ modes are, in a way, interchanged, when the critical speed is crossed. Thus, according to Fig. 9 , it is advantageous, from the rotordynamic viewpoint, to have a minor constant for the subcritical motors, and large time constant for the supercritical motors. The effect of $\tilde{\tau}_{p\pm1}$ on the damping of backward whirling mode is minor (see Figs. 4 and 5).

The last electromagnetic parameter γ is connected to the slip. It determines the resonance frequencies together with the supply frequency and the number of pole-pairs. This parameter appears to have a minor effect on the vibration behaviour on the electromechanical system.

4. Discussion and conclusions

A new simple model was presented to assess the effects of electromechanical interaction on the rotordynamics of cage induction motors. The model was obtained by combining the Jeffcott rotor model with a simple electromagnetic force model including two additional variables for the harmonic currents of the rotor cage. The parameters of this electromechanical rotor model have

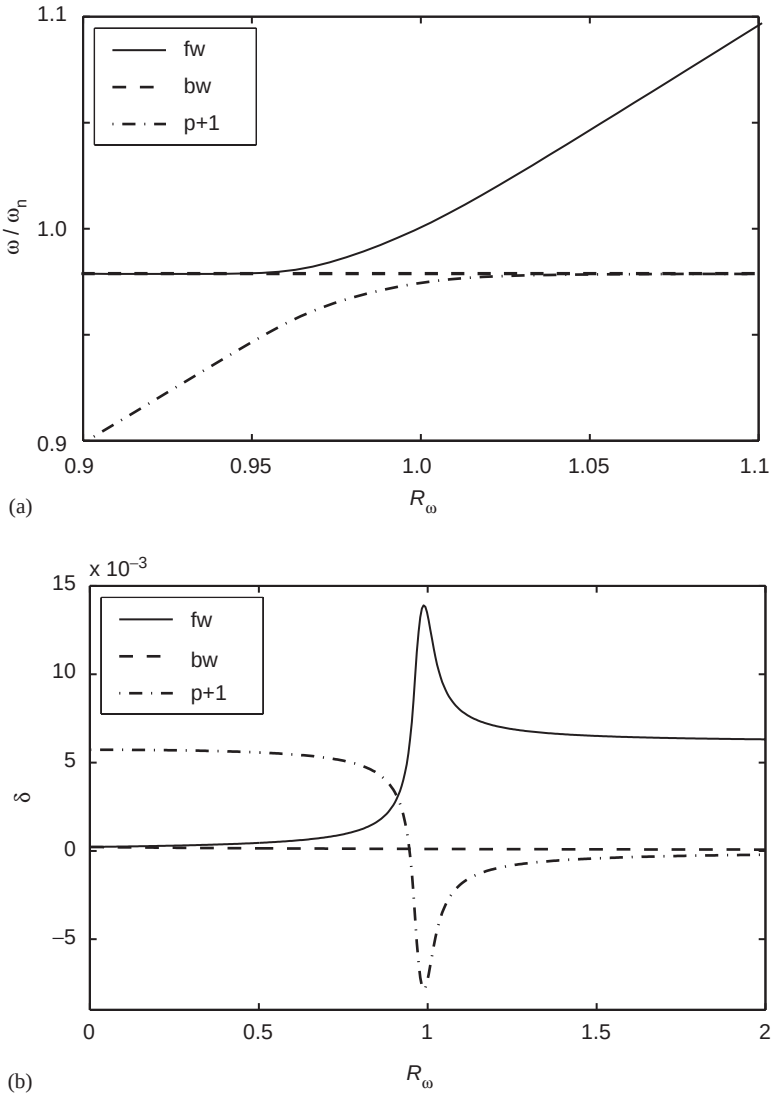

Fig. 4. Dimensionless eigenfrequencies (a) and decay constants (b) of the 2.6 MW two-pole motor as a function of rotation speed in the stator reference frame. The labels of the modes are connected to the forward whirling (fw), backward whirling (bw), and harmonic cage current $p+1$ at the lower end of rotation speed. The constant parameters are: $\alpha = 0.111$, $\tilde{c}_{p+1} = 0.623$, $\tilde{\tau}_{p+1} = 162$, $\zeta_e = 0$.

clear physical meaning. The parameter values of a motor can be estimated from the design data, or from the numerical simulation results, as was done in this study. To generalise the results and observations, the electromechanical rotor model was transformed into a dimensionless form.

The purely mechanical Jeffcott rotor model includes the forward and backward whirling modes. The electromagnetic force model increases the total number of modes by two. In principle, all the modes of the electromechanical rotor model are coupled electromechanical modes. However, the interaction between the mechanical and electrical system is strong only when the

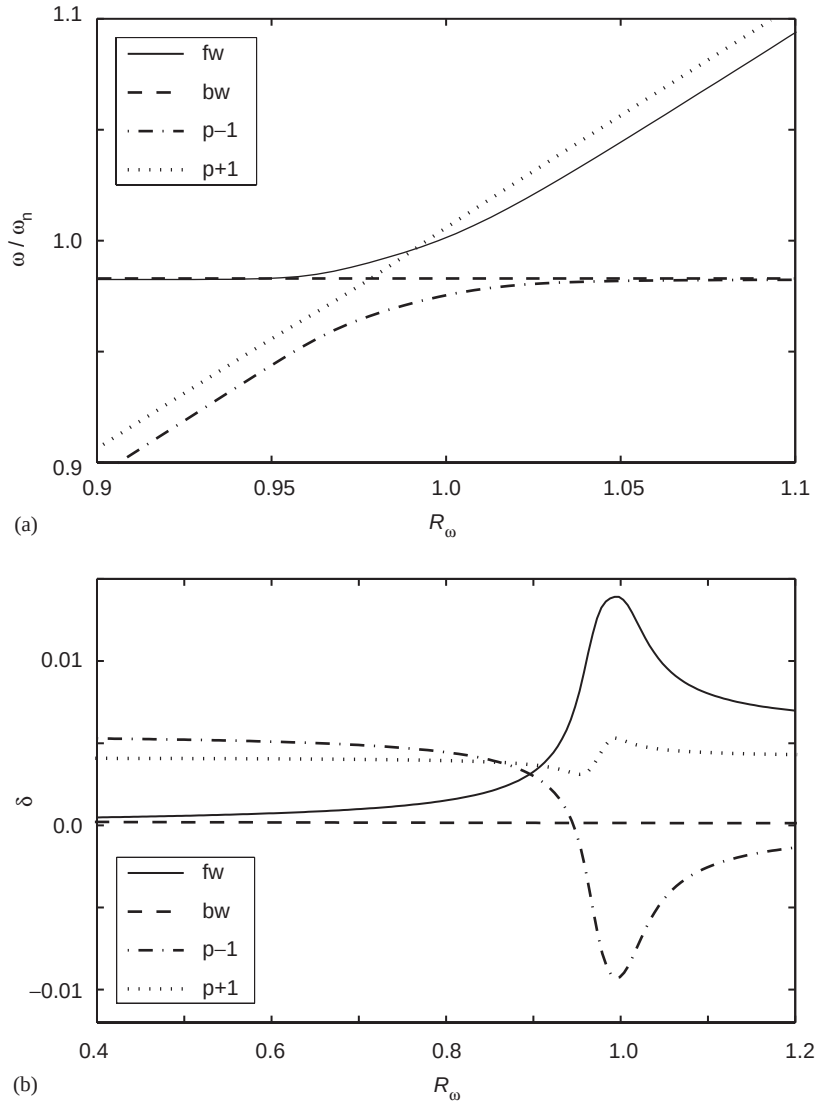

Fig. 5. Dimensionless eigenfrequencies (a) and decay constants (b) of the 4.2 MW four-pole motor as a function of rotation speed ratio in the stator reference frame. The constant parameters are: $\alpha = 0.134$, $\tilde{c}_{p-1} = 0.126$, $\tilde{c}_{p+1} = 0.616$, $\tilde{\tau}_{p-1} = 240$, $\tilde{\tau}_{p+1} = 169$, $\zeta_e = 0$.

rotor rotational speed is close to the first bending critical speed. In that case, the originally electromagnetic modes may couple with the forward whirling mode.

In conclusion, the electromechanical interaction decreases the natural frequencies of the rotor. This effect is known as the electromagnetically induced negative spring constant [2,3]. At subcritical rotational speeds, the mechanical vibration energy of all modes is dissipated via resistive losses of the cage currents, or transformed into a form of electrical energy. At supercritical rotational speeds, the effects are qualitatively similar with the exception of one mode,

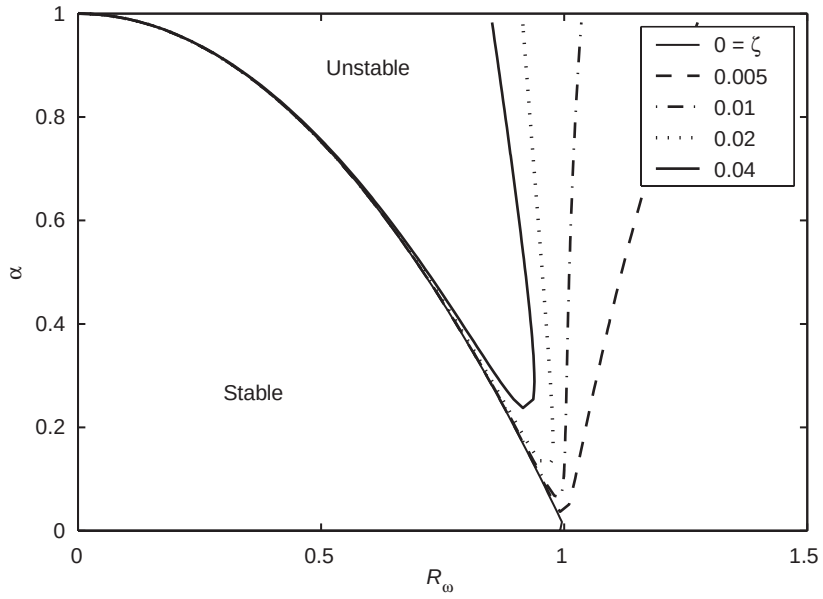

Fig. 6. Stability chart for the speed ratio (R_ω), force ratio (α) and external damping (ζ). The reference point taken from the parameters of the 2.6 MW motor: $\tilde{c}_{p+1} = 0.623$, $\tilde{\tau}_{p+1} = 162$.

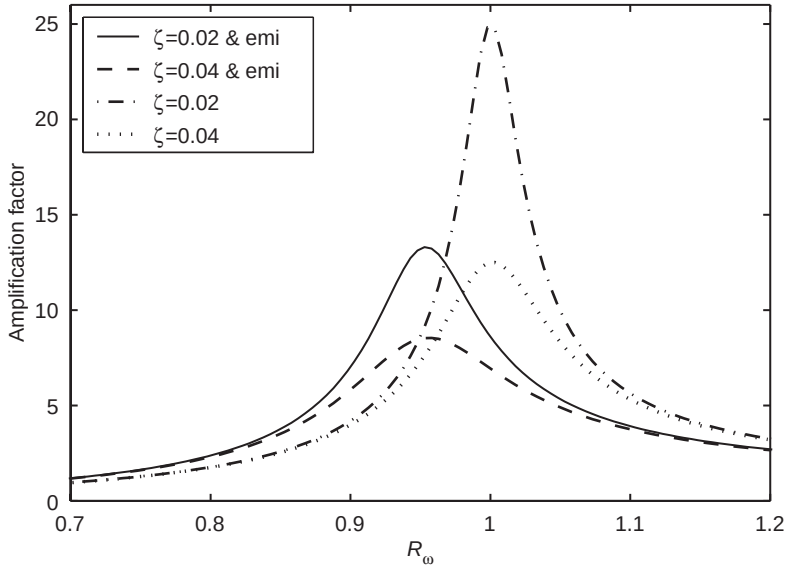

Fig. 7. Amplification factor due to the mass unbalance. The amplification factor using two different non-rotating damping factors are calculated together with electromechanical interaction (emi) or without it. The other parameters are taken from the 2.6 MW motor: $\alpha = 0.111$, $\tilde{c}_{p+1} = 0.623$, $\tilde{\tau}_{p+1} = 162$.

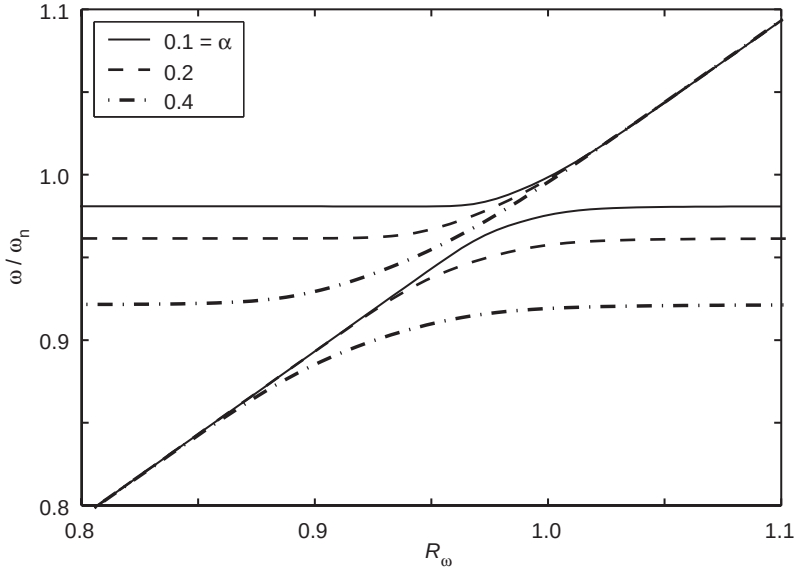

Fig. 8. Dimensionless eigenfrequencies for the forward whirling (up on the left) and the $p+1$ modes (down on the right) with three different α coefficient. The parameters of the 2.6 MW two-pole motor are used for the other parameters: $\tilde{c}_{p+1} = 0.623$, $\tilde{\tau}_{p+1} = 162$, $\zeta_e = 0$, $\gamma = 0.00379$.

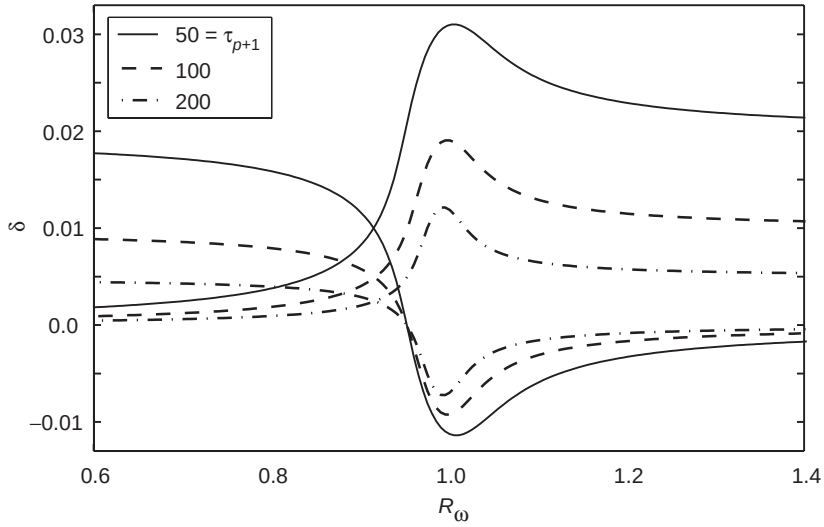

Fig. 9. Dimensionless decay constants for the forward whirling (up on the right) and the $p+1$ modes (down on the right) with three different $\tilde{\tau}_{p+1}$ coefficients. The parameters of the 2.6 MW two-pole motor are used for the other parameters: $\alpha = 0.111$, $\tilde{c}_{p+1} = 0.623$, $\zeta_e = 0$, $\gamma = 0.00379$.

which receives energy from the electrical system. If the mechanical energy dissipation of this mode is too small, a form of self-excited vibrations may follow leading to the rotordynamic instability. Because this instability is induced by the periodic variation of the system parameters (Eq. (3)), this

phenomenon is one form of the parametric instability [16]. Excluding the potential rotordynamic instability, the numerical results indicate that the electromechanical interaction reduces effectively the unbalance response close to the first bending critical speed.

In this study, the rotor core was assumed to be rigid and perfectly aligned with the rigid stator bore. These assumptions enabled the use of the two-dimensional electromagnetic models, and restricted the rotor model and induced vibrations to be symmetric. Secondly, the homopolar flux may have remarkable effects on the vibrations of flexible-shaft two-pole motors [3] . However, in this study, the homopolar flux was ignored in the estimation of electromechanical force parameters. Thirdly, the presented results are limited to the cage induction motors without parallel paths in the stator windings. It is assumed that the parallel paths affect the interaction forces resembling the effects of rotor cage currents by enabling circulatory currents in the stator winding. Fourthly, only the low-order components of the eccentricity harmonics $p \pm 1$ were included into the parametric force model. The high-order components may induce significant force components, particularly at higher frequencies.

Acknowledgements

The authors gratefully acknowledge the financial support of the National Technology Agency of Finland (Tekes). Special thanks are due to Mr. P. Klinge, VTT Industrial Systems, for reviewing the manuscript and making valuable suggestions.

References

[1] W. Freise, H. Jordan, Einseitige magnetische Zugkräfte in Drehstrommaschinen, *Elektrotechnische Zeitschrift: ETZ, Ausgabe A* 83 (1962) 299–303.
[2] J. Früchtenicht, H. Jordan, H.O. Seinsch, Exzentrizitätsfelder als Ursache von Laufinstabilitäten bei Asynchronmaschinen, Part 1 and 2, *Archiv für Electrotechnik* 65 (1982) 271–292.
[3] R. Belmans, A. Vandenput, W. Geysen, Influence of unbalanced magnetic pull on the radial stability of flexible-shaft induction machines, *IEE Proceedings, Part B* 134 (1987) 101–109.
[4] D.Yu. Skubov, I.V. Shumakovich, Stability of the rotor of an induction motor in the magnetic field of the current windings, *Mechanics of Solids* 34 (1999) 28–40 (Translated from *Mekhanika Tverdogo Tela* (1999) 36–50).
[5] A. Arkkio, M. Antila, K. Pokki, A. Simon, E. Lantto, Electromagnetic force on a whirling cage rotor, *IEE Proceedings—Electric Power Applications* 147 (2000) 353–360.
[6] T.P. Holopainen, A. Tenhunen, E. Lantto, A. Arkkio, Unbalanced magnetic pull induced by arbitrary eccentric motion of cage rotor in transient operation. Part 1: analytical model, *Electrical Engineering*, in press.
[7] D. Childs, *Turbomachinery Rotordynamics: Phenomena, Modeling, and Analysis*, Wiley, New York, 1993.
[8] A. Arkkio, *Analysis of Induction Motors Based on the Numerical Solution of the Magnetic Field and Circuit Equations*, Finnish Academy of Technology, Helsinki, 1987. (Acta Polytechnica Scandinavia, Electrical Engineering Series, No. 59) http://lib.hut.fi/Diss.
[9] J.L. Coulomb, A methodology for the determination of global electromechanical quantities from a finite element analysis and its application to the evaluation of magnetic forces, torques and stiffness, *IEEE Transactions on Magnetics* 19 (1983) 2514–2519.
[10] P.K. Kovács, *Transient Phenomena in Electrical Machines*, Elsevier, Amsterdam, 1984.
[11] D.J. Ewins, *Modal Testing: Theory, Practice and Application*, 2nd Ed., Research Studies Press, Hertfordshire, England, 2000.

[12] T.P. Holopainen, A. Tenhunen, E. Lantto, A. Arkkio, Unbalanced magnetic pull induced by arbitrary eccentric motion of cage rotor in transient operation. Part 2: verification and numerical parameter estimation, *Electrical Engineering*, in press.
[13] A. Tenhunen, T.P. Holopainen, A. Arkkio, Impulse method to calculate the frequency response of the electromagnetic forces on whirling cage rotors, *IEE Proceedings—Electric Power Applications* 150 (2003) 752–756.
[14] T.P. Holopainen, A. Tenhunen, E. Lantto, A. Arkkio, Numerical identification of electromagnetic force parameters for linearized rotordynamic model of cage induction motors, *Journal of Vibration and Acoustics* 126 (2004) 384–390.
[15] L. Meirovitch, *Principles and Techniques of Vibrations*, Prentice-Hall, Englewood Cliffs, NJ, 1997.
[16] M.A. Prohl, F.F. Ehrich, D.W. Childs, Vibration considerations in the design of rotating machinery, in: F.F. Ehrich (Ed.), *Handbook of Rotordynamics*, McGraw-Hill, New York, 1992, pp. 1.1–1.155.